PAPER

A comparative study of electrochemical cells for *in situ* x-ray spectroscopies in the soft and tender x-ray range

To cite this article: Juan-Jesús Velasco-Vélez *et al* 2021 *J. Phys. D: Appl. Phys.* **54** 124003

View the article online for updates and enhancements.

You may also like

A comparative study of electrochemical cells for *in situ* x-ray spectroscopies in the soft and tender x-ray range

Juan-Jesús Velasco-Vélez[1] , **Lorenz J Falling**[1] , **Denis Bernsmeier**[2], **Michael J Sear**[3], **Pip C J Clark**[3], **Ting-Shan Chan**[4], **Eugen Stotz**[1], **Michael Hävecker**[1,5], **Ralph Kraehnert**[2], **Axel Knop-Gericke**[1,5], **Cheng-Hao Chuang**[6] , **David E Starr**[3], **Marco Favaro**[3] and **Rik V Mom**[1,7]

[1] Fritz Haber Institute of the Max Planck Society, Faradayweg 4-6, 14195 Berlin, Germany
[2] Technische Universität Berlin, Institut für Chemie, Str. des 17. Juni 124, 10623 Berlin, Germany
[3] Helmholtz-Zentrum Berlin für Materialien und Energie GmbH, Institute for Solar Fuels, Hahn-Meitner-Platz 1, 14109 Berlin, Germany
[4] National Synchrotron Radiation Research Center, Hsinchu 30076, Taiwan
[5] Max Planck Institute for Chemical Energy Conversion, Stiftstrasse 34-36, 45413 Mülheim an der Ruhr, Germany
[6] Department of Physics, Tamkang University, No. 151 Yingzhuan Rd, New Taipei City 25137, Taiwan
[7] Leiden Institute of Chemistry, Leiden University, PO Box 9502, 2300 RA Leiden, The Netherlands

E-mail: r.v.mom@lic.leidenuniv.nl

CrossMark

Abstract

In situ x-ray spectroscopies offer a powerful way to understand the electronic structure of the electrode–electrolyte interface under operating conditions. However, most x-ray techniques require vacuum, making it necessary to design spectro-electrochemical cells with a delicate interface to the wet electrochemical environment. The design of the cell often dictates what measurements can be done and which electrochemical processes can be studied. Hence, it is important to pick the right spectro-electrochemical cell for the process of interest. To facilitate this choice, and to highlight the challenges in cell design, we critically review four recent, successful cell designs. Using several case studies, we investigate the opportunities and limitations that arise in practical experiments.

Supplementary material for this article is available online

(Some figures may appear in colour only in the online journal)

1. Introduction

X-ray spectroscopies rank among the most powerful characterization techniques in a physical chemist's toolbox. Depending on the particular implementation, one can gain access to e.g. oxidation states, the local electrostatic potential (e.g. band bending), and the density of states around the Fermi level. For electrochemists, such insights into the electronic structure of

materials strongly complement the kinetic and thermodynamic information that can be acquired using classical current–voltage measurements.

Ideally, spectroscopy and electrochemistry are combined into a single *in situ* spectroscopy experiment. This allows one to identify the dynamics of the electrode and (near-surface) electrolyte as a function of the applied potential. For example, *in situ* x-ray spectroscopy has successfully revealed reactive
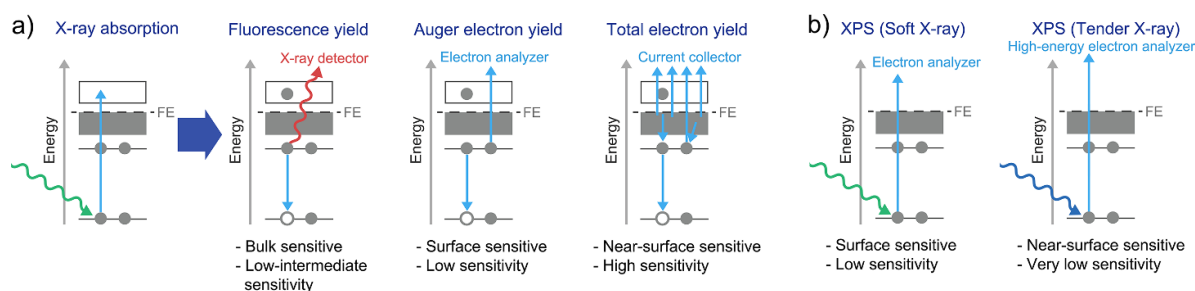
Figure 1. Fundamentals of *in situ* XAS and XPS. (a) X-ray absorption detection modes used with the cells compared here. (b) Concept of XPS. FE designates the Fermi energy.

oxygen species during the oxygen evolution reaction [1–6], the distribution of the electrostatic potential in the electric double layer [7] and the oxidation state of Cu electrodes during the reduction of CO_2 [8, 9]. However, *in situ* x-ray spectroscopy is technically challenging, particularly for the soft/tender x-ray regime that is required for the best chemical sensitivity. The fundamental challenge is that low-energy x-rays and photoelectrons can only travel a short distance through a solid or liquid without inelastic scattering: 1–100 μm for x-rays [10] and 0.5–50 nm for electrons [11, 12]. Hence, to probe the buried electrode–electrolyte interface, one has to minimize the thickness of either the electrode or the electrolyte, or both.

In recent years, a variety of spectro-electrochemical cells have been developed for soft and tender x-ray spectroscopies [13–27], primarily for use at synchrotron facilities. The designs differ strongly in how the electrochemical cell is interfaced with the vacuum or He-filled detection chamber surrounding it. In addition, the electrode–electrolyte interface is sometimes probed from the electrode side, and sometimes from side of the electrolyte. Each of these approaches imposes restrictions on factors such as the types of samples, electrolytes and spectroscopic techniques that can be used. Furthermore, there is significant variation in performance and practical applicability of the methods. Due to the complexity of electrochemical x-ray spectroscopy and its limited availability, experimenters tend to focus on a single preferred technique and an overview of the various approaches is lacking. Therefore, this manuscript provides a comprehensive comparison of four successful methods for *in situ* x-ray absorption spectroscopy (XAS) and *in situ* x-ray photoelectron spectroscopy (XPS). Using several case studies, we critically review the capabilities and limitations of the techniques, providing a set of practical considerations for the selection of the right cell for the electrochemical process of interest.

2. Cell description

In this section, we provide a general description of the four types of spectro-electrochemical cells compared in this work. Details about the sample preparation and the specific implementation of the cells used for data acquisition can be found in supporting information (SI) section S1 (available online at stacks.iop.org/JPD/54/124003/mmedia).

2.1. Techniques and detection methods

Although a wide variety of x-ray spectroscopies is possible in the four cells considered here, we will focus on XAS and XPS. *In situ* XAS measurements can be performed via several detection modes (see figure 1(a)), which vary in their advantages and the restrictions they impose on the cell design. Absorption can be detected directly, by measuring the transmission through thin sample/electrolyte layers [24, 28], or indirectly by detecting the photoelectrons [2–4, 21, 29, 30] or fluorescent x-rays [4, 8, 9, 17, 25, 31] that are emitted as a result of the absorption process. For electron detection, one can distinguish between Auger electron yield-XAS and total electron yield-XAS (TEY-XAS). In the former, an electron energy analyzer is used to selectively detect Auger electrons. TEY-XAS does not have this selectivity, but rather detects all electrons that escape from the sample (i.e. primary, Auger, and secondary electrons). Not all cells can use all detection methods, as will be discussed below.

In situ XPS makes use of an electron analyzer to measure the kinetic energy of emitted photoelectrons (figure 1(b)). Regular electron analyzers require high vacuum in the spectroscopy chamber, which is difficult to combine with electrochemical cells. Therefore, near-ambient-pressure analyzers are typically used instead, allowing for pressures up to 5–50 mbar in the spectroscopy chamber. Both soft and tender x-rays can be used in the measurements. In general, soft x-rays ($\sim$0.1–2 keV) enable better surface sensitivity, whereas tender x-rays ($\sim$2–10 keV) are better for the study of buried layers and interfaces. Note that tender x-ray XPS is usually referred to as HAXPES. Finally, note that the cells discussed here are designed for applications in the energy range from $\sim$0.3 to 5 keV, whereas other approaches are more effective for energies above 5 keV [20, 32–34].

2.2. SiN$_x$ window cell

The most commonly used cell type for *in situ* x-ray spectroscopy experiments is shown in figure 2(a). In this design, the working electrode is deposited onto a thin window with excellent x-ray transparency. Commonly used window materials are SiN$_x$, SiC, Kapton, or Mylar with a thickness of $\sim$100–500 nm, depending on the photon energy range that is used. The electrochemical interface is probed through the
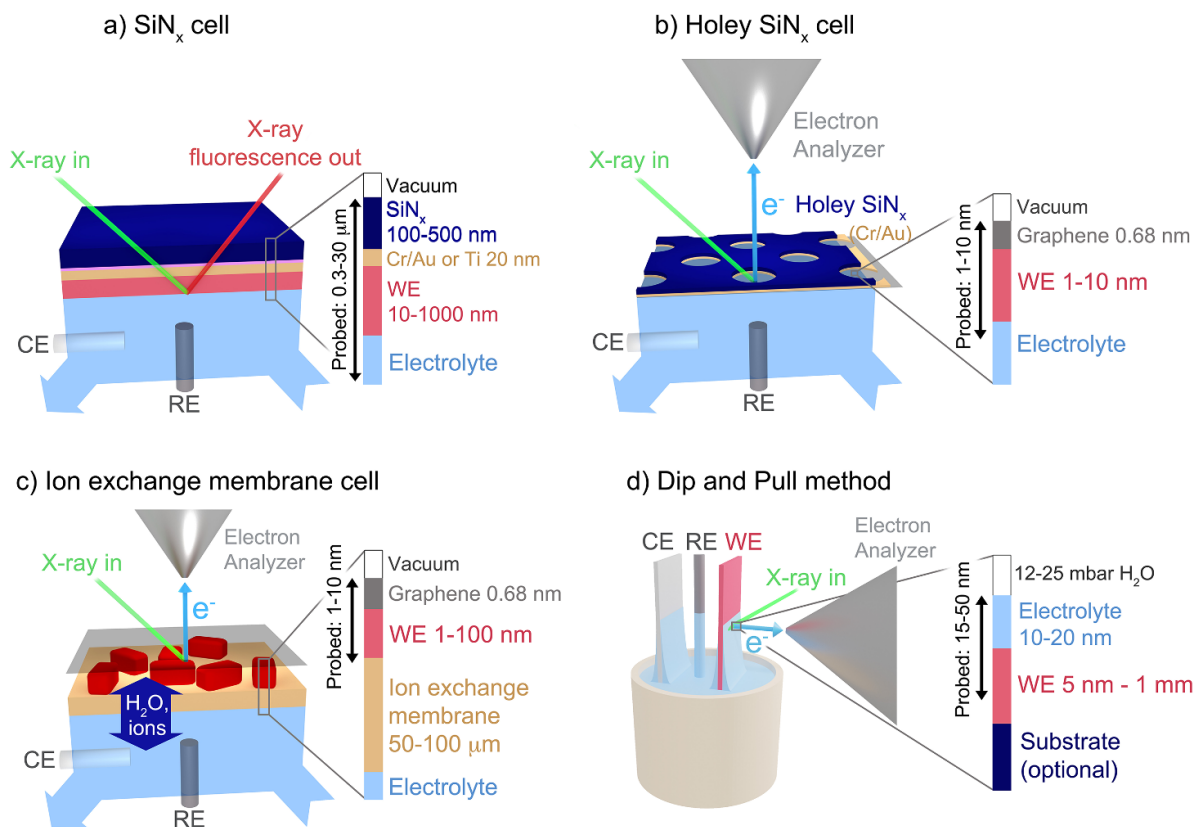
J. Phys. D: Appl. Phys. **54** (2021) 124003

J-J Velasco-Vélez *et al*

Figure 2. Spectro-electrochemical cells considered in the comparison. (a) SiN$_x$ flow cell for fluorescence yield XAS. (b) Holey SiN$_x$ flow cell for XPS and electron yield XAS. (c) Ion exchange membrane flow cell for XPS and electron yield XAS. (d) Dip and pull method for XPS and electron yield XAS. CE, RE and WE correspond to counter electrode, reference electrode and working electrode, respectively.

window and the working electrode, which is usually porous. For the typical window thickness of 100–500 nm, no photoelectrons can escape the cell. For this reason, the SiN$_x$ window cell is typically used for bulk-sensitive photon in/photon out techniques such as fluorescence yield XAS [25, 26, 31, 35] and (resonant) x-ray emission spectroscopy [17, 26]. In our case, we used XAS with total fluorescence yield detection (figure 1(a)), which has a probing depth in the micrometer range.

2.3. Holey SiN$_x$ cell

To enable surface sensitive methods in the SiN$_x$ cell geometry, a different type of window is used: holey SiN$_x$ covered with a double layer of graphene [21, 36]. As shown in figure 2(b), the holes in the SiN$_x$ membrane are covered only by graphene, which has a high electron transparency [21, 36–38]. This allows for XPS and electron-yield XAS (figure 1(a)) measurements with a probing depth in the range of 1–10 nm.

2.4. Ion exchange membrane (IEM) cell

The use of membrane electrode assemblies is a common strategy in industrial electrochemistry to separate gases formed or consumed at the cathode and anode (e.g. electrolyzers [39, 40], fuel cells [41], and chlorine production [40]). Recently, it was shown that one can also make use of such

membrane-supported electrodes for *in situ* XAS and XPS experiments [2, 4, 18, 29]. As shown in figure 2(c), the working electrode is deposited on an ion-conducting membrane, which is in contact with flowing electrolyte on the back. This ensures the transport of water and ions to and from the working electrode. To minimize water evaporation into the vacuum of the spectroscopy chamber, the working electrode is covered by a graphene (double)layer. This enables the formation of an ultrathin liquid electrolyte layer around the working electrode [2, 18, 29]. The graphene layer also provides electrical contact when dispersed nanoparticles are studied, and is meanwhile transparent to x-rays and even photoelectrons down to 200 eV [18]. This, and the modest pressure in the chamber of 0.03–0.2 mbar, enables surface sensitive electron yield XAS and XPS measurements with soft x-rays in a near-ambient pressure XPS set-up.

2.5. Dip and pull method

The dip and pull method and its analogues [23, 42–44] enable XPS and electron yield XAS studies of the solid–liquid interface by minimizing the electrolyte layer thickness. As shown in figure 2(d), an electrolyte beaker with three electrodes is placed in a vacuum chamber. To reduce water evaporation, the chamber pressure is kept at 12–25 mbar and an additional water source is added. To start the experiment, the three electrodes are dipped deep into the electrolyte solution, and then

Table 1. Suitable sample morphologies for *in situ* x-ray spectroscopy.

Cell type	Allowed sample morphologies
SiN$_x$ cell	(Porous) Thin films
Holey SiN$_x$ cell	Graphene, graphene-supported nanoparticles/porous thin films
Ion exchange membrane cell	Graphene, graphene-supported nanoparticles/porous thin films
Dip and pull method	Anything macroscopically flat, e.g. (layered) films, foils, single crystals

partially pulled back out again. This procedure often leaves an electrolyte film on the working electrode that is tens of nanometers thick. This is thick enough to reach bulk-like behavior in the film [45], yet thin enough to still detect XPS signal from the working electrode, provided that excitation energies of more than 2 keV are used. This is accomplished in modern tender x-ray near-ambient-pressure XPS endstations [11].

2.6. Samples that can be used

The cell designs in figure 2 impose restrictions on the types of samples that can be used. The allowed sample morphologies are summarized in table 1. For the cells where the electrode–electrolyte interface is probed from the electrode side, only nanoparticles or thin films can be used. Because the interface is probed from the electrolyte side in the dip and pull method, it imposes less restrictions on the electrode morphology. The only requirement is that a continuous thin electrolyte film can be created on the electrode surface by the dip and pull motion, which is ensured by having a macroscopically flat sample (microscopic roughness is generally acceptable).

Tailoring the electrode morphology to the *in situ* experiment can be a powerful way to optimize spectroscopic performance, while also ensuring realistic and reproducible electrochemistry. For example, well-defined mesoporous oxide films with controlled crystallinity and templated mesopore structure have proven to be excellent model materials to study phase transformations, gas–solid interactions or electrocatalysis [46–51]. Along these lines, we will study mesoporous RuO$_x$. In addition, we will study two other commonly used electrode materials: IrO$_x$ and graphene. In section 3, we will discuss how the morphology of the electrode materials affects what we can observe in the spectroscopy.

2.7 Where can the cells be used

At present, the availability of facilities where the spectro-electrochemical cells can be used is rather limited. With the exception of an analogue of the dip and pull method [44], all facilities are located at synchrotrons. That said, the SiN$_x$ cell is offered for beamlines in the soft and tender x-ray range at a variety of synchrotrons all over the world. The dip and pull method, too, is available at several beamlines in Europe and the US (BL 9.3.1 at ALS, KMC-1 at BESSY II, PHOENIX I at SLS, HIPPIE at MAXIV). The characteristics of these

beamlines show significant variation in energy range, beam spot size, and facilities for sample preparation, providing some flexibility to match the beamline with the intended experiment. Such flexibility is not available for the IEM cell and the holey SiN$_x$ cell, which are currently only offered at the ISISS beamline at BESSY II.

We should note that there are currently several initiatives running to implement the cells at more beamlines. Hence, we expect that their availability will strongly increase in the near future. This will also bring new possibilities, such as the combination of soft and tender x-ray measurements at CAT at BESSY II. Instrumentation for electrochemical XPS outside the synchrotron is also under development.

3. Results

3.1. Electrochemical response

To study an electrochemical process using spectroscopy, an important requirement is that the electrochemistry at the measurement spot is well-controlled. For the SiN$_x$ and holey SiN$_x$ cells, this is intrinsically ensured because the working electrode is in direct contact with flowing bulk electrolyte. Indeed, the cyclic voltammogram (CV) of IrO$_x$ on SiN$_x$ in 0.1 M H$_2$SO$_4$ (figure 3(a)) is in excellent agreement with those obtained in regular cells [18, 52]. This indicates that the potential control and proton transport were not impeded by the cell geometry.

In the IEM cell, water and ions are transported to and from the working electrode through the support membrane. Unsurprisingly, this works very well for proton transport through a Nafion membrane widely used in acid electrolysis, resulting in a good CV (figure 3(b)). Under these conditions, an ohmic drop of 40–70 Ω is typically measured between the working and reference electrode. A more challenging test in terms of mass transport is the electrodeposition of Cu, where ion concentrations are lower and large Cu^{2+} ions have to be transported. As shown in figure 3(c), this is still no problem for the SiN$_x$ cell, which shows the usual onset potential [53] and high currents. In contrast, the IEM cell requires significant overpotential to achieve a modest deposition current, even though we employed a membrane optimized for cation transport. Whether this transport limitation for larger ions is general for the IEM cell remains to be seen, but it is clear that for the polymer IEMs employed so far, the electrolyte needs to be chosen with some care.

Not all aspects of the electrochemical response of the cells can be readily probed using classical current–voltage measurements, because the measurement spot may behave differently than other parts of the electrode. This can sometimes occur in the IEM cell, where the side of the electrode that is in contact with the IEM can behave differently than the side that is probed in the spectroscopy (see figure 2(c)). This situation occurs when the electrolyte transport through the electrode layer is impeded. We recently exemplified an extreme case of this using Pt electrodes with and without the graphene cover layer [29]. When no graphene cover is present, the electrolyte in the catalyst layer evaporates. Therefore, there is almost no
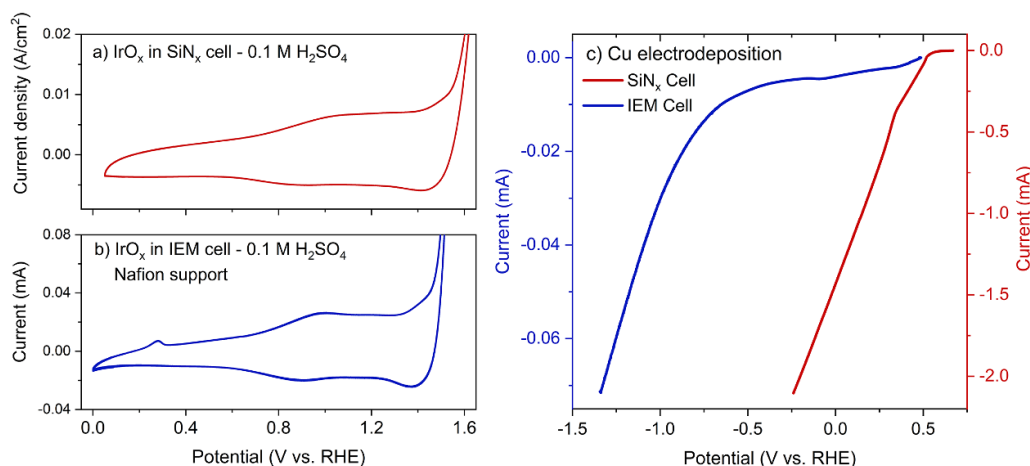
J. Phys. D: Appl. Phys. **54** (2021) 124003

J-J Velasco-Vélez *et al*

Figure 3. Electrochemical characterization of the SiN$_x$ and ion exchange membrane (IEM) cell. (a), (b) Cyclic voltammograms recorded *in situ*. (c) Linear sweep voltammograms recorded in 50 mM CuSO$_4$. For the SiN$_x$ cell, 20 nm Au on 2 nm Cr/SiN$_x$ was used as the electrode. For the IEM cell the graphene cover layer served as the electrode, with a Fumatech FKD cation exchange membrane as the support.
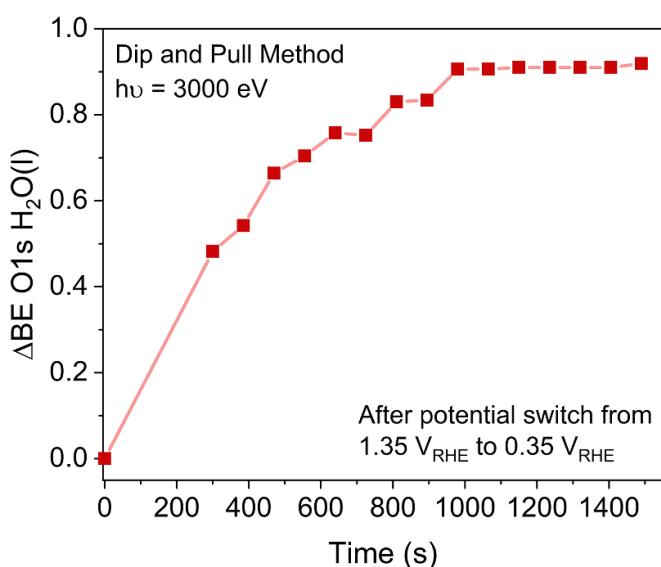

Figure 4. Equilibration of a 10–15 nm 0.1 M H$_2$SO$_4$ film on mesoporous RuO$_x$ following a potential step. The O1s peak position is used to track the electrolyte potential.

ion transport to and from the top of the electrode, which is probed by XPS. As a result, very little response to the applied potential was observed in the XPS spectra. In contrast, when a sample with graphene cover was studied, oxidation/reduction of the top of the Pt electrode could readily be observed. From this example, it is clear that good transport through the catalyst layer is important for IEM cell experiments. This can be ensured by using sufficiently open/porous electrode layers and a good quality graphene evaporation barrier. As will be shown in figure 6, electrochemical response on the order of seconds can be achieved if these conditions are met (see also [2, 29]). Note, however, that electrode layers with pores/cracks of only a few nm in size generally do not operate well in very low concentration electrolytes due to insufficient screening [54].

Hence, the electrolyte concentration that can be used in IEM cell experiments depends on the electrode morphology.

Local differences in electrochemical response are also a concern in the dip and pull method, where reactants have to be transported from the beaker to the measurement spot through the 10–30 nm electrolyte film on the working electrode (see figure 2(d)). As can be expected from such a geometry, recent modeling showed that transport perpendicular to the electrode is fast (i.e. from film to electrode), but transport along the parallel to the electrode is much slower (i.e. from beaker to measurement spot) [55]. To assess this experimentally, we studied the equilibration of a 0.1 M H$_2$SO$_4$ film on a mesoporous RuO$_x$ electrode following a potential jump from 1.35 V$_{RHE}$ to 0.35 V$_{RHE}$. During this potential jump, proton adsorption occurs on the RuO$_x$ electrode (details in next section). Because this is a very fast reaction, the equilibration process will be limited by the proton transport along the electrolyte film. As long as the proton concentration in the film is depleted, the electrode potential will not be properly screened by the electrolyte film. This screening can be probed using XPS, by tracking the position of the O1s peak of liquid water, which shifts along with the electrostatic potential in the film [7]. As shown in figure 4, it takes more than 15 min for the electrolyte potential to equilibrate completely. This confirms that transport parallel to the solid–electrolyte interface is strongly limited in the dip and pull geometry, even for protons. For dip and pull studies on continuous reactions such as electrodeposition or electrocatalysis, the consequence is that reactants are depleted at the measurement position, whereas products are in excess. In addition, the potential that is effectively applied can deviate locally in some cases, depending on the nature of the reaction and the supporting electrolyte [56]. Hence, data on continuous reactions should be interpreted with caution. In contrast, studies of the electrode–electrolyte interface under static conditions are not affected by the mass transport limitations.
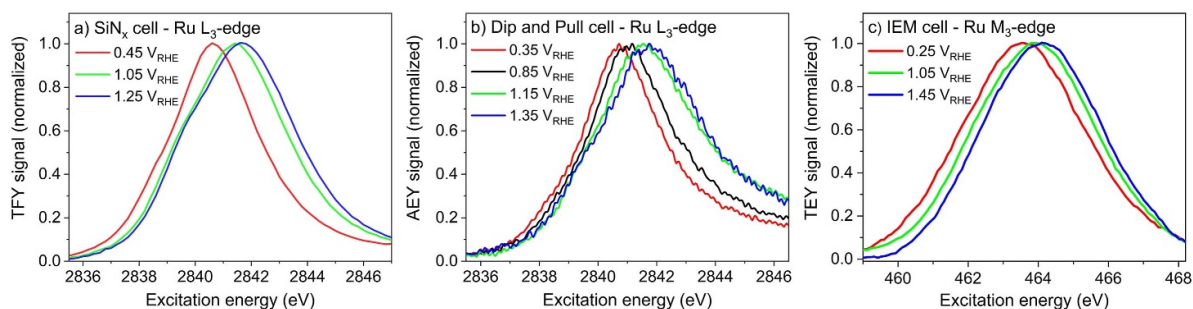
J. Phys. D: Appl. Phys. **54** (2021) 124003

J-J Velasco-Vélez *et al*

Figure 5. *In situ* XAS measurements on mesoporous RuO$_x$ in the SiN$_x$, dip and pull, and ion exchange membrane (IEM) cell geometry, with 0.1 M H$_2$SO$_4$ as the electrolyte. The RuO$_x$ layer thickness was about 140 nm for the SiN$_x$ cell, and 70 nm for the other cells. Nafion 117 was used as the support membrane for the IEM cell. The employed detection modes are indicated on the *y*-axes.

3.2. Characterizing electrodes using XAS and XPS

In situ XAS and XPS have been used to study a variety of electrode materials, ranging from metal single crystals to oxide nanoparticles [2, 4, 5, 21, 23, 29, 53, 57, 58]. Here, we will explore the possibilities for XAS and XPS measurements using the case study of RuO$_x$ and IrO$_x$.

3.2.1. XAS. First, we have studied the electronic structure of ruthenium in mesoporous RuO$_x$ using XAS. The porous structure of the RuO$_x$ gives it an exceptionally high surface-to-bulk ratio (see figure S1 in the SI), making it relatively easy to detect changes in the surface and near-surface structure of the electrode. As shown in figure 5, we indeed had no trouble observing changes in the electronic structure of Ru when ramping up the electrode potential. During this potential increase, OH groups are deprotonated:

$$Ru - OH \rightarrow Ru - O + H^+ + e^-. \tag{1}$$
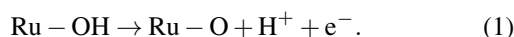
At low potentials, when many OH groups are present, the XAS resonance (i.e. peak) shape and position is consistent with Ru^{3+} [59, 60]. At higher potentials, the peak shifts to higher excitation energy and shows a more pronounced shoulder (t$_{2g}$ contribution), which is typical of Ru^{4+} [60, 61]. Hence, it appears that when the RuO$_x$ is deprotonated, an oxidation of Ru^{3+} to Ru^{4+} occurs.

While this chemical change is clearly visible for all cells, there are also differences in the measurements. For the dip and pull cell, only the AEY detection mode was available, which often provides a relatively low signal-to-noise ratio. Hence, figure 5(b) shows clear noise. We expect that this could be remedied by introducing the TEY detection mode to dip and pull beamlines, which would require minimal adjustments. For the SiN$_x$ cell, only fluorescence yield detection is possible. This works quite well in the tender x-ray range, resulting in good quality Ru L$_3$-edge spectra (figure 5(a)). However, note that a relatively thick 140 nm RuO$_x$ layer was needed to reach this quality. This requirement can be problematic for studies on materials that do not come in mesoporous form: If only the top few atomic layers participate in the electrochemistry, a non-porous sample would show almost exclusively inactive bulk signal. This is different for the IEM cell, which typically uses AEY or TEY detection that only probes the top few nanometer of the electrode [62]. Because the IEM cell is installed on a soft x-ray beamline, we recorded the Ru M$_3$-edge rather than the L$_3$-edge (figure 5(c)). While this edge has weaker features than the L$_3$-edge, it does allow us to show the efficiency of the TEY detection mode: the M$_3$-edge was recorded in ∼15 s, versus ∼10 min for figure 5(a) and ∼30 min for figure 5(b). Note that the efficiency of the beamline software (availability of 'on-the-fly' measurement) and the desired signal-to-noise ratio also play a role in this.

In our comparison, we were not able to include the holey SiN$_x$ cell due to the challenge of preparing the mesoporous RuO$_x$ layer in this geometry. However, previous experiments on Co electrodeposition have shown that its performance is rather similar to the IEM cell [21].

While the data in figure 5 shows the capabilities of *in situ* XAS under static conditions, time-resolved measurements are also possible. We will showcase this using the IEM cell. Figure 6(a) shows how deprotonation of amorphous ruthenium oxide is visible in O K-edge spectra. To follow the deprotonation during a potential sweep, we measured the AEY signal at 529 eV (figure 6(b)) during the potential program in figure 6(c). As expected from the CV (see figure S2 in the SI), deprotonation is detected over a wide potential range. In many cases, the excitation energy at which an OH group shows its main O K-edge resonance (peak) depends on its coordination number (e.g. μ_1–OH, μ_2–OH). Hence, one can perform the XAS tracking experiments at multiple excitation energies to detect the potential range for the deprotonation of different OH groups [2].

3.2.2. XPS. The mesoporous RuO$_x$ samples were also investigated using XPS (figures 7(a) and (b)). Similar to the XAS case, we find a clear response to the applied potential. Notice in figure 7(a) that there is a uniform response, i.e. the Ru 3d$_{5/2}$ peak shifts as a whole rather than that it splits into multiple contributions. This implies that all the Ru atoms that we detect respond in the same way, i.e. that Ru^{3+}/Ru^{4+} redox occurs over the entire XPS probing depth. Using Shard's nanoparticle method [63, 64] and the 'S3 equation' [11], we estimate that 80% of the signal comes from the top 1.1 nm of the sample (details in SI section S2.1). Hence, Ru redox proceeds at least several (hydr)oxide layers into the material.
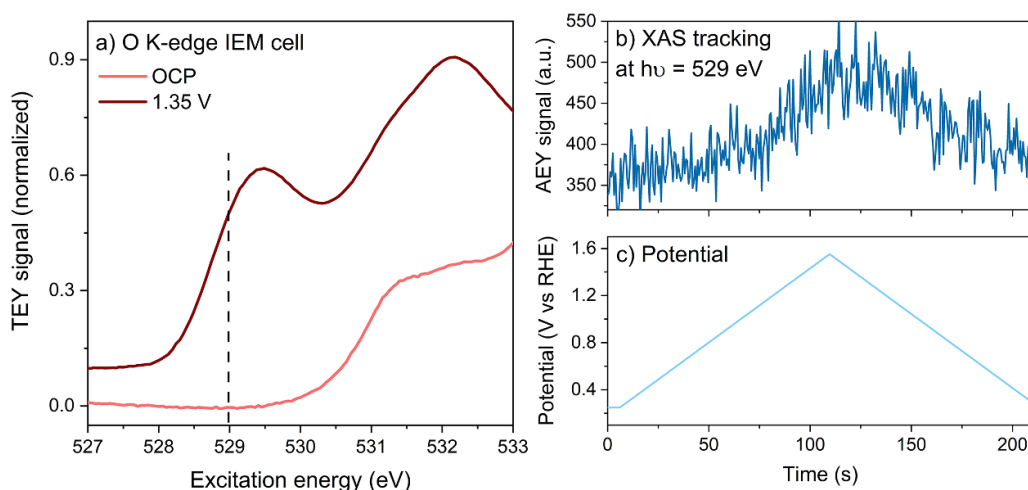
Figure 6. Deprotonation of amorphous ruthenium oxide on Nafion 117 in 0.1 M H_2SO_4 followed using the O K-edge in the IEM cell. (a) Measurements under static conditions. The dashed line indicates the excitation energy used for the tracking measurements in (b), which probe the level of deprotonation during the potential program in (c).
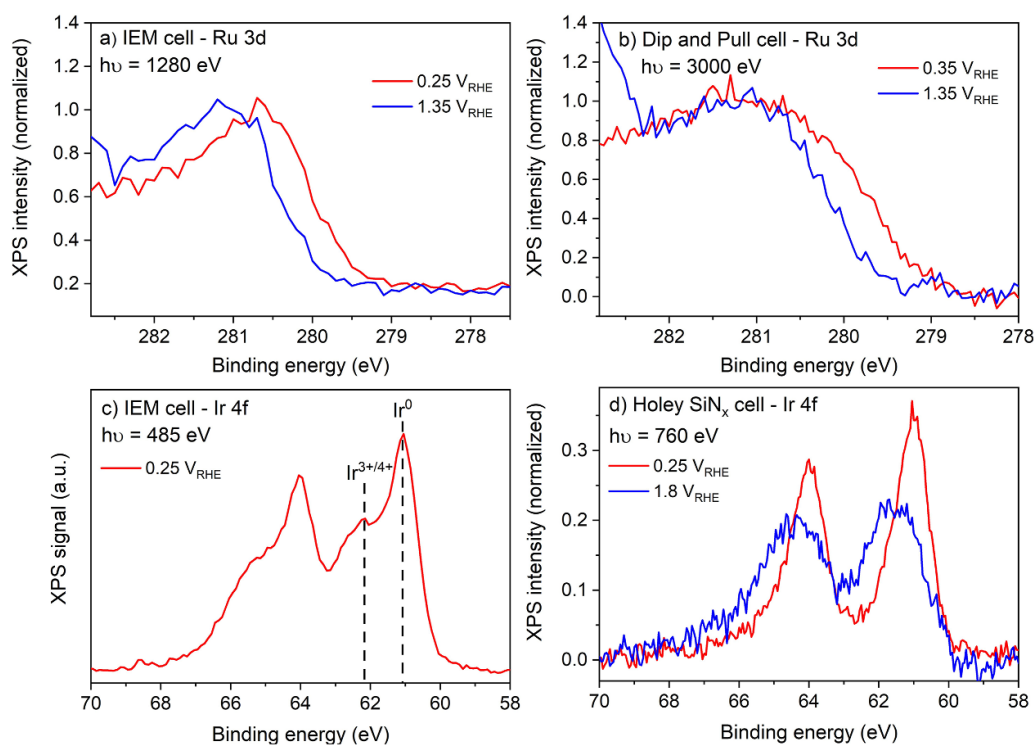

Figure 7. *In situ* XPS measurements on (a), (b) mesoporous RuO_x and (c), (d) Ir , with 0.1 M H_2SO_4 electrolyte. The data is shown after Shirley background subtraction. Nafion 117 was used as the support membrane for the IEM cell.

Since the dip and pull method uses tender x-ray XPS (HAXPES), which probes deeper into the material, we can use it to see if the Ru redox proceeds all the way through the bulk. From figure 7(b), it is clear that this is not the case. At low potential, a very broad peak is observed, implying a mixed Ru^{3+}/Ru^{4+} oxidation state. At high potential, the peak width decreases, suggesting a uniform Ru^{4+} oxidation state. Hence, there appears to be a core of Ru^{4+} ions that does not respond to the applied potential, and an outer layer that adopts a Ru^{3+} or Ru^{4+} oxidation state depending on the conditions. Based

on the probing depth in the dip and pull experiment (80%@ 1.9 nm), we estimate the outer layer to be about 1.1–1.3 nm thick. Note that the Ru^{3+} and Ru^{4+} contributions should also appear in the XAS results. However, the broad, smooth shape of the Ru L- and M-edges makes it challenging to disentangle multiple contributions.

The case of Ru redox above shows the power of the Dip and Pull method to probe buried layers, making it very suitable to study the near-surface of electrodes, or layered nano-devices (e.g. photo-electrocatalysis). On the other hand, there are also
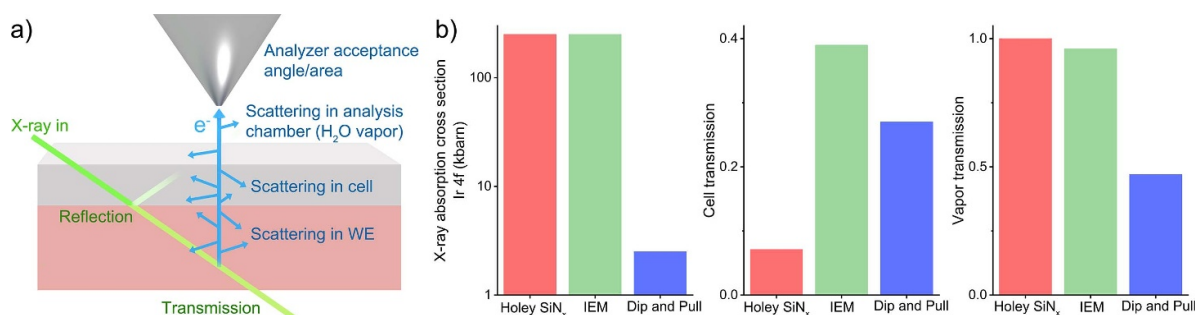
Figure 8. Loss factors for *in situ* XPS. (a) Depiction of loss factors. (b) Quantification of important loss factors for typical experimental conditions (details in SI section S2.2).

cases where the redox process of interest is restricted to the surface. In such cases, it is important to maximize the surface sensitivity of the measurement. This is exemplified in figure 7(c), which shows the Ir 4f spectrum of an Ir film oxidized in 30% H_2O_2 prior to the *in situ* experiment. This oxidation treatment is insufficient to reach deep into the film, creating only a surface oxide layer. Nonetheless, it is possible to clearly distinguish the oxide and metal contributions in the spectrum obtained using the IEM cell. This was achieved by using a low x-ray energy (485 eV), which creates low-energy photoelectrons ($\sim$420 eV) that can only escape from the top few atomic layers of the electrode. Such low x-ray energies are not possible using the dip and pull method, where an x-ray energy around 3000 eV is usual. Under typical measurement conditions, the oxide signal would contribute only $\sim$8% of the total Ir 4f intensity with this x-ray energy. From this example, it is clear that probing surface reactions can be challenging with the dip and pull method in its present state, whereas the IEM method excels at this point. A future direction to close this gap in surface sensitivity would be the use of grazing incidence x-rays ($\sim$0.5° incidence) in the dip and pull geometry [65].

Good surface sensitivity can also be achieved using the holey SiN_x cell, as it allows for measurements with rather low x-ray energies. In the example shown in figure 7(d), for instance, 80% of the signal comes from the top 0.43 nm of the $\sim$2.1 nm Ir nanoparticles (details in SI section S2.1). At open circuit potential (0.25 V_{RHE}), only the metallic state is detected within this probing depth, showing that the particles do not significantly oxidize without applied potential, in good agreement with previous results [2, 66]. Raising the potential to 1.8 V_{RHE}, where the oxygen evolution reaction occurs, oxidizes the particles. However, the broad Ir 4f peak shape shows that the particles have not completely oxidized within the time frame of the experiment. Again, this showcases the ability of XPS to separate core and shell contributions under electrochemical conditions.

From figure 7, it should be clear that useful XPS data can be obtained in all cell configurations, but with varying surface or buried layer sensitivity. We should note that there are also variations in the acquisition speed and typical spectral resolution. The origin of these differences can mainly be found in the x-ray absorption cross section, photoelectron scattering, and the beamline/acquisition characteristics. As shown in figure 8, the HAXPES used in the dip and pull method suffers from

rather low x-ray absorption cross sections [67, 68] (note the logarithmic scale in figure 8(b)), meaning that relatively few photoelectrons are generated within the XPS probing depth. From the electrons emitted by the electrode, a significant fraction is scattered in the cell (electrolyte film) or in the H_2O vapor of the analysis chamber. Scattering in the cell is also important for the holey SiN_x cell, where photoelectrons can only escape from the holes in the SiN_x membrane, which cover just 18%–20% of the beam footprint. A more comprehensive discussion of all factors that determine the XPS sensitivity is provided in SI section S2.2.

The loss factors above can be compensated in several ways. Most importantly, the acquisition time is adjusted: About 15–20 min per spectrum is normal for the dip and pull method, 5–10 min for the holey SiN_x cell and 1–2 min for the IEM cell. Additional signal intensity can be obtained by increasing the pass energy of the electron analyzer, although this can have a negative impact on the spectral resolution. In general, the resolution of the measurements is determined by a combination of the beamline characteristics and the electron analyzer settings. Tender x-ray beamlines often offer somewhat lower resolution than soft x-ray beamlines, but there is no general rule.

3.3. Characterizing the electric double layer

Most *in situ* XPS and XAS studies so far have focused on the dynamics of electrodes in various electrochemical processes. However, possibilities also exist to characterize the electrolyte near the interface, i.e. the electric double layer [7, 29]. The structure of this double layer is extremely difficult to probe using other methods, and has therefore remained one of the most elusive aspects in our understanding electrochemistry [69]. In figure 9, we show the XPS signals from sulfate and potassium ions, obtained in the dip and pull cell and the holey SiN_x cell, respectively. In both cases, a clear response to the applied potential is observed. A large part of this response can be linked back to changes in the electrostatic potential of the ions. The connection between binding energy and electrolyte potential is explained in figure 10. When the working electrode is grounded to the XPS set-up, the electrolyte potential with respect to the set-up will move up or down with the applied potential. This translates directly into the observed binding energy according to
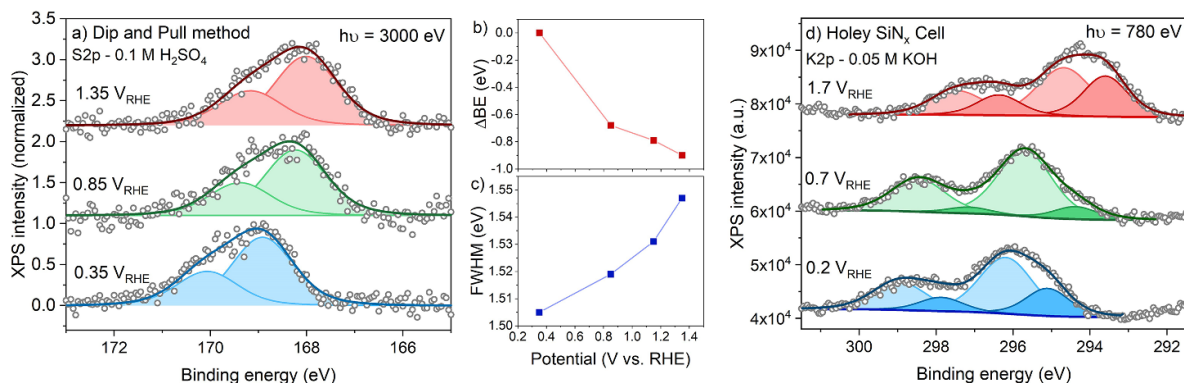
Figure 9. XPS spectra of ions near the electrochemical interface. (a)–(c) S2p spectrum of a 10–15 nm 0.1 M H_2SO_4 electrolyte film on mesoporous RuO_x. ΔBE and FWHM designate binding energy shift and full width at half maximum of the fitted peaks, respectively. (d) K2p spectra of 0.05 M KOH in contact with a graphene electrode. Both S2p and K2p spectra were fitted using doublets with an LF Gaussian-Lorentzian line shape and fixed spin-orbit splitting of 1.15 eV and 2.77 eV, respectively. Note that the working electrode was grounded to the XPS set-up during the experiments.
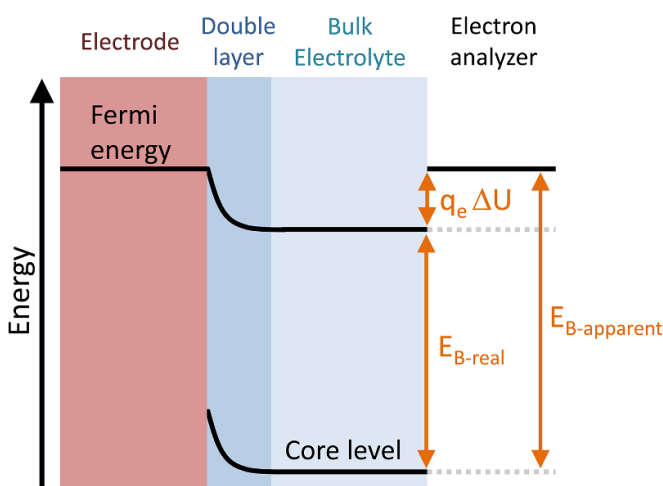

Figure 10. Effect of the electrolyte potential ΔU on the observed binding energy. $E_{B\text{-real}}$, $E_{B\text{-apparent}}$, and q_e designate the 'real' binding energy, the apparent/observed binding energy, and the charge of an electron, respectively.

$$E_{B\text{-apparent}} = E_{B\text{-real}} + q_e \Delta U. \qquad (2)$$

Here, $E_{B\text{-apparent}}$ designates the observed binding energy, $E_{B\text{-real}}$ the 'real' binding energy, q_e the charge of an electron, and ΔU the electrolyte potential versus the working electrode. If we consider the idealized situation of an electrolyte with uniform potential and no specific electrode–electrolyte interactions, than the XPS peaks of the electrolyte will simply shift 1 to -1 with the applied potential, without any change in peak shape. The situation in figures 9(a)–(c) is quite close to this case. When the working electrode potential is increased by 1 V, there is a peak shift of -0.9 eV. Meanwhile, the peak shape changes only marginally. This suggests that the electric double layer, where the electrolyte potential deviates from the bulk value (see figure 10), has a modest contribution to the observed spectra.

We can rationalize the double layer contribution if we consider the dip and pull cell geometry. As shown in figure 2(d),

the electrode–electrolyte interface is probed through an electrolyte film. Due to scattering of the photoelectrons, the top of the 10–15 nm electrolyte film contributes more to the signal than the bottom, i.e. the electric double layer. If we model this situation with a flat electrode, a uniform ion concentration, and a double layer of 1 nm thick, the double layer will only contribute some 3%–6% to the total signal (model details in SI Section 2.1). Hence, double layer experiments using the dip and pull approach need to take specific precautions. In our case, we opted for using a mesoporous electrode, which greatly increases the probed electrode–electrolyte interface area, especially if we consider that tender x-ray XPS also probes inside the mesopores. The fact that we still see only a minor double layer contribution suggests that the double layer is much thinner than 1 nm for 0.1 M H_2SO_4 @ RuO_x, in line with simulations on other electrolytes [70]. Being able to establish this experimentally is a new avenue in electrochemical research, which complements classical capacitance measurements that indirectly probe the double layer. To further improve dip and pull measurements on the double layer thickness and composition, thinner electrolyte layers and lower ion concentration (thicker double layer) [7] could be employed.

Following the example of the dip and pull method, we also used the holey SiN_x cell to conduct double layer measurements. As shown in figure 9(d), double layer effects are clearly observed for 0.05 M KOH @ graphene. The presence of multiple doublets in the K2p spectrum points at specific chemical interactions between potassium and the graphene electrode. Meanwhile, the peak position of the darker colored component did not follow a steady 1:-1 shift as a function of applied potential. Hence the electrolyte potential within the XPS probing depth was not uniform, indicating that the potential decay in the double layer was probed. This can be expected, because the holey SiN_x cell probes the electrolyte from the electrode side, i.e. the side of the double layer. If we again model the double layer contribution using a flat electrode, uniform ion concentration, and a double layer thickness of 1 nm, we expect a contribution of 29%. This number could

J. Phys. D: Appl. Phys. **54** (2021) 124003

J-J Velasco-Vélez *et al*

be further increased by lowering the excitation energy. This makes the holey SiN$_x$ cell a very powerful tool for double layer studies. However, note that a uniform double layer is only reached for graphene electrodes. If nanoparticles of another material are deposited on the graphene window, a double layer will form at both this material and at the graphene window, both of which are probed by XPS. These signals would have to be disentangled, for example by varying the nanoparticle coverage.

Detecting electrolyte species is also possible in the IEM cell [18, 29]. However, the IEM itself is generally also part of the double layer [29], making its description more complex. Finally, there is no principle reason why XAS measurements on double layer species cannot be performed in all four cells. However, with double layer characterization still in an early phase, only few studies have done this so far [30, 71].

3.4. Challenges in sample preparation and operation

Although the data and considerations provided here showcase the detailed knowledge that can be obtained using *in situ* x-ray spectroscopies, we should point out that these are not routine, 'plug and play' experiments. First, the sample preparation route often needs to be tailored to the restrictions imposed by the employed cell. Second, bringing the cell into measurement conditions may require great care. In this section, we discuss the typical challenges encountered during preparation and operation.

3.4.1. SiN$_x$ cell.
Because popular x-ray window materials like SiN$_x$ and Kapton show weak interaction with most materials, it can be challenging to create a well-dispersed sample layer on them that will not delaminate during operation. To improve adhesion and ensure uniform electrical contact, the windows are often coated with Ti or Cr Au [17, 25, 35]. The catalyst layer is usually applied by a technique that ensures uniform deposition, such as dip-coating (this manuscript), physical/chemical vapor deposition [9], or electrodeposition [8, 53]. Drop casting of powders is also possible, but obtaining a thin, stable layer is generally more challenging in our experience. Due to the high chemical and thermal stability of SiN$_x$ and Kapton, calcination or heat treatments at temperatures up to at least 400 °C are possible even after deposition. A final consideration is that due to the bulk sensitivity of fluorescence yield XAS measurements performed with this cell, one should employ either very thin or porous electrodes to be sufficiently sensitive to the electrode–electrolyte interface.

Especially for SiN$_x$, the window is usually only 100–500 nm thick, which means that it is fragile. Hence, care must be taken when bringing such windows into vacuum and when filling the cell with electrolyte. An additional challenge is that any bubbles in the electrolyte stream or formed at the electrode are likely to be trapped in the channel leading to the x-ray window, thus blocking electrolyte access to the sample. The bubbles can only be removed by pulsing the electrolyte flow or emptying and refilling the cell. These procedures again may lead to rupture of the x-ray window. When the cell is used in

a high vacuum chamber (rather than a He-filled or near ambient pressure chamber), there are also strict requirements on its leak tightness.

Like with all x-ray techniques, beam damage needs to be considered in the measurements. This holds particularly for soft x-rays, since they have stronger interaction with matter than tender or hard x-rays. The SiN$_x$ cell itself is not affected by extended x-ray exposure. However, some electrocatalysts are susceptible to beam damage. In general, this should be tested *in situ*. Furthermore, the beam exposure per area should be minimized, either by using a large beam spot size or by moving the beam spot around.

3.4.2. Holey SiN$_x$ cell.
The preparation of samples for this cell type requires significant skill. First, the quality of the graphene layer needs to be excellent, covering all holes in the SiN$_x$ membrane without tears or pinholes. This should be checked using scanning electron microscopy to ensure a reasonable success rate in the XPS experiments. In our experience, only a double layer of graphene provides sufficient stability and the holes in the SiN$_x$ membrane should not exceed 1.3 μm diameter. Deposition of the material of interest onto the graphene window has been performed using electrodeposition [21] and physical vapor deposition [66]. Note that calcination of the samples is limited to about 200 °C in order to prevent damage to the graphene layer.

The resulting samples are highly fragile. Therefore, a limited fraction will survive pumping down ($\sim$90%) and sustained operation in the vacuum chamber over the course of hours ($\sim$10%). Applying oxidizing potentials (e.g. oxygen evolution reaction regime) and extended x-ray exposure shortens the expected lifetime of the samples. The sample lifetime may also be strongly affected by the strain exerted by mounting it onto the cell. Due to the small area of the hole array in the SiN$_x$ membrane, the possibilities for minimizing beam damage by moving the x-ray spot are limited.

3.4.3. IEM cell.
In the IEM cell, the graphene cover layer serves as an evaporation barrier, which stabilizes the electrolyte film around the working electrode [2, 18, 29]. To make this evaporation barrier function properly, it is essential to ensure that lateral transport of water to defects in the graphene (leak sites) is minimized. In addition, every XPS/XAS spectrum needs to be recorded in a fresh spot to mitigate beam damage to the IEM, which is often quite sensitive [18, 29]. These restrictions necessitate the use of thin ($\sim$1–100 nm), homogeneous sample layers. This has been achieved successfully for physical vapor deposition [2, 29], electrodeposition [18], drop casting [4], and hot pressing (this manuscript). For samples that require calcination, the sample layer needs to be prepared on a different substrate (e.g. glassy carbon, soluble crystals) and subsequently transferred onto the polymer membrane. For all samples, the final step is the deposition of graphene. Although this procedure is unfamiliar to most electrochemists, it is readily set up in any lab [18, 36, 72].

The operation of the IEM cell is the easiest among the compared cells, because the cell is robust. The only points of care

Table 2. Summary of pros and cons of the four investigated spectro-electrochemical cells. Scores are indicated as $++$ (excellent/easy), $+$ (good/fairly easy), $\pm$ (acceptable/somewhat challenging), and $-$ (poor/challenging).

Cell type	Techniques		What can be probed				Practical aspects				
	XAS	XPS	Electrode surface	Burried layers	Double layer	Mass transport	Sample flexibility	Ease of prep.	Ease of operation	XPS quality	XAS quality
SiN$_x$	Yes	No	$\pm$	$+$	$-$	$++$	$\pm$	$\pm$	$\pm$	n/a	$+$
Holey SiN$_x$	Yes	Yes	$++$	$-$	$++$	$++$	$-$	$-$	$-$	$+$	$+$
Ion exchange membrane	Yes	Yes	$++$	$-$	$\pm$	$\pm$	$\pm$	$\pm$	$++$	$++$	$++$
Dip and pull	Yes	Yes	$+$	$++$	$+$	$-$	$++$	$+$	$+$	$+$	$\pm$

are to ensure that no bubbles are trapped on the backside of the membrane, and that beam damage to the membrane is minimized by limiting the measurement time per spot [18, 29].

3.4.4. Dip and pull cell. The dip and pull method imposes essentially no restrictions on the sample preparation. The only limitation is that the sample needs to be sufficiently large and macroscopically flat to establish a well-defined meniscus. The principle of operation in dip and pull experiments is fairly straightforward as well. However, establishing a stable meniscus of 10–30 nm thick can be challenging, especially for non-wetting, flat samples like noble metal foils. Care must also be taken to ensure that the electrolyte film remains connected to the bulk electrolyte (no gap in the film), which can be ensured by measuring the local electrostatic potential of the electrolyte via the 0 1 s peak of liquid water. Like for the other cells, beam damage should be considered. However, the use of tender x-rays generally limits this aspect. Finally, care must be taken to degas the electrolyte. Electrolyte sucked into the analyzer during the splash of a bursting bubble may cause damage to the system.

4. Conclusion

With the case studies presented here, we have showcased how both electrodes and near-surface electrolyte can be studied in detail using *in situ* XAS and XPS. The pros and cons of the four spectro-electrochemical cells that we considered are summarized in table 2.

Although all cells can handle a wide range of applications, it should be clear that they have very different strengths:

- The SiN$_x$ cell (figure 2(a)) offers good mass transport, but is mainly suitable for bulk sensitive fluorescence-yield XAS. Therefore, its ideal use case is to study electrocatalytic reactions on porous electrodes with high surface area.
- The key attraction of the holey SiN$_x$ cell (figure 2(b)) is that it combines measurements in bulk electrolyte with surface sensitive measurements (XPS, electron-yield XAS). However, the cell is highly fragile and accepts a limited range of materials. Therefore, we estimate that its best use case is for dedicated studies on the electric double layer and electrode–electrolyte interactions at graphene or graphene-supported nanoparticle electrodes.
- The IEM cell (figure 2(c)) is highly robust and also offers surface sensitive measurements. However, mass transport is limited for larger ions. Since this cell employs membrane-electrode assemblies by design, its best use case is to study processes where such assemblies are used in practice (e.g. electrolyzers, fuel cells).
- The dip and pull cell is the most flexible in terms of samples and is very suitable to probe buried layers. While the other cells are limited to nanoparticles and/or thin films, the dip and pull cell can also handle different sample forms such as thick films, layered structures, and single crystals. It particularly excels for the study of layered structures,

such as those in photo-electrocatalytic devices, where probing buried layers is important. Its main disadvantage is its extremely limited mass transport parallel to the surface in the electrolyte film.

Finally, we should note that our study shows the current state-of-the-art in a field that is in rapid development. Based on the progress made over the last 10 years, we expect that many of the challenges highlighted here will be tackled in the coming years. The critical view presented here can serve as an inspiration in this development.

ORCID iDs

Juan-Jesús Velasco-Vélez ⓘ https://orcid.org/0000-0002-6595-0168
Lorenz J Falling ⓘ https://orcid.org/0000-0002-2622-5166
Cheng-Hao Chuang ⓘ https://orcid.org/0000-0001-8161-1521
Marco Favaro ⓘ https://orcid.org/0000-0002-3502-8332
Rik V Mom ⓘ https://orcid.org/0000-0002-5111-5591

References

[1] Pfeifer V, Jones T E, Velasco-velez J J, Arrigo R, Piccinin S, Hävecker M, Knop-gericke A and Schlögl R 2017 *In situ* observation of reactive oxygen species forming on oxygen-evolving iridium surfaces *Chem. Sci.* **8** 2143–9

[2] Frevel L, Mom R V, Velasco-velez J J, Plodinec M, Knop-Gericke A and Schlögl R 2019 *In situ* x-ray spectroscopy on the electrochemical development of iridium nanoparticles in confined electrolyte *J. Phys. Chem. C* **123** 9146–52

[3] Saveleva V A, Wang L, Teschner D, Jones T, Gago A S, Friedrich K A, Zafeiratos S, Schlögl R and Savinova E R 2018 Operando evidence for a universal oxygen evolution mechanism on thermal and electrochemical iridium oxides *J. Phys. Chem. Lett.* **9** 3154–60

[4] Tesch M F *et al* 2019 Evolution of oxygen–metal electron transfer and metal electronic states during manganese oxide catalyzed water oxidation revealed with *in situ* soft x-ray spectroscopy *Angew. Chem. Int. Ed.* **58** 3426–32

[5] Yoshida M, Mitsutomi Y, Mineo T, Nagasaka M, Yuzawa H, Kosugi N and Kondoh H 2015 Direct observation of active nickel oxide cluster in nickel-borate electrocatalyst for water oxidation by *in situ* O K-edge x-ray absorption spectroscopy *J. Phys. Chem. C* **119** 19279–86

[6] Drevon D, Görlin M, Chernev P, Xi L, Dau H and Lange K M 2019 Uncovering the role of oxygen in Ni-Fe(OxHy)

J. Phys. D: Appl. Phys. **54** (2021) 124003

J-J Velasco-Vélez *et al*

electrocatalysts using *in situ* soft x-ray absorption spectroscopy during the oxygen evolution reaction *Sci. Rep.* **9** 1–11

[7] Favaro M, Jeong B, Ross P N, Yano J, Hussain Z, Liu Z and Crumlin E J 2016 Unravelling the electrochemical double layer by direct probing of the solid/liquid interface *Nat. Commun.* **7** 12695

[8] Velasco-Vélez J J *et al* 2019 The role of the copper oxidation state in the electrocatalytic reduction of CO_2 into valuable hydrocarbons *ACS Sustain. Chem. Eng.* **7** 1485–92

[9] Chou T C *et al* 2020 Controlling the oxidation state of the Cu electrode and reaction intermediates for electrochemical CO_2 reduction to ethylene *J. Am. Chem. Soc.* **142** 2857–67

[10] Henke B L, Gullikson E M and Davis J C 1993 X-ray interactions: photoabsorption, scattering, transmission, and relfection at E=50-30,000 eV, Z=1-92 *At. Data Nucl. Data Tables* **54** 181–342

[11] Seah M P 2012 Simple universal curve for the energy-dependent electron attenuation length for all materials *Surf. Interface Anal.* **44** 1353–9

[12] Cumpson P J and Seah M P 1997 Elastic scattering corrections in AES and XPS. II. Estimating attenuation lengths and conditions required for their valid use in overlayer/substrate experiments *Surf. Interface Anal.* **25** 430–46

[13] Nemšák S *et al* 2018 In aqua electrochemistry probed by XPEEM: experimental setup, examples, and challenges *Top. Catal.* **61** 2195–206

[14] Arrigo R, Hävecker M, Schuster M E, Ranjan C, Stotz E, Knop-gericke A and Schlögl R 2013 *In situ* study of the gas-phase electrolysis of water on platinum by NAP-XPS *Angew. Chem. Int. Ed.* **52** 11660–4

[15] Guay D, Stewart-Ornstein J, Zhang X and Hitchcock A P 2005 *In situ* spatial and time-resolved studies of electrochemical reactions by scanning transmission x-ray microscopy *Anal. Chem.* **77** 3479–87

[16] Guo J 2013 The development of *in situ* photon-in/photon-out soft x-ray spectroscopy on beamline 7.0.1 at the ALS *J. Electron Spectros. Relat. Phenom.* **188** 71–78

[17] Asakura D *et al* 2015 Operando soft x-ray emission spectroscopy of $LiMn_2O_4$ thin film involving Li-ion extraction/insertion reaction *Electrochem. Commun.* **50** 93–96

[18] Falling L J *et al* 2020 Graphene-capped liquid thin films for electrochemical operando x-ray spectroscopy and scanning electron microscopy *ACS Appl. Mater. Interfaces* **12** 37680–92

[19] Velasco-Velez J-J *et al* 2020 Revealing the active phase of copper during the electroreduction of CO_2 in aqueous electrolyte by correlating *in situ* x-ray spectroscopy and *in situ* electron microscopy *ACS Energy Lett.* **5** 2106–11

[20] Masuda T and Uosaki K 2017 *In situ* determination of electronic structure at solid/liquid interfaces *J. Electron Spectros. Relat. Phenom.* **221** 88–98

[21] Velasco-velez J J *et al* 2015 Photoelectron spectroscopy at the graphene—liquid interface reveals the electronic structure of an electrodeposited cobalt/graphene electrocatalyst *Angew. Chem. Int. Ed.* **54** 14554–8

[22] Masuda T, Yoshikawa H, Noguchi H, Kawasaki T, Kobata M, Kobayashi K and Uosaki K 2013 *In situ* x-ray photoelectron spectroscopy for electrochemical reactions in ordinary solvents *Appl. Phys. Lett.* **103** 111605

[23] Axnanda S *et al* 2015 Using 'tender' x-ray ambient pressure x-ray photoelectron spectroscopy as a direct probe of solid-liquid interface *Sci. Rep.* **5** 09788

[24] Nagasaka M, Yuzawa H, Horigome T and Kosugi N 2014 In operando observation system for electrochemical reaction by soft x-ray absorption spectroscopy with potential modulation method *Rev. Sci. Instrum.* **85** 104105

[25] Braun A, Sivula K, Bora D K, Zhu J, Zhang L, Grätzel M, Guo J and Constable E C 2012 Direct observation of two electron holes in a hematite photoanode during photoelectrochemical water splitting *J. Phys. Chem.* C **116** 16870–5

[26] Schwanke C, Golnak R, Xiao J and Lange K M 2014 Electrochemical flowcell for *in-situ* investigations by soft x-ray absorption and emission spectroscopy *Rev. Sci. Instrum.* **85** 103120

[27] Casalongue H S, Kaya S, Viswanathan V, Miller D J, Friebel D, Hansen H A, Nørskov J K, Nilsson A and Ogasawara H 2013 Direct observation of the oxygenated species during oxygen reduction on a platinum fuel cell cathode *Nat. Commun.* **4** 2817

[28] Schwanke C, Xi L and Lange K M 2016 A soft XAS transmission cell for operando studies *J. Synchrotron Radiat.* **23** 1390–4

[29] Mom R, Frevel L, Velasco-Velez J J, Plodinec M, Knop-gericke A and Schlögl R 2019 The oxidation of platinum under wet conditions observed by electrochemical x-ray photoelectron spectroscopy *J. Am. Chem. Soc.* **141** 6537–44

[30] Velasco-Velez J J, Wu C H, Pascal T A, Wan L F, Guo J, Prendergast D and Salmeron M 2014 The structure of interfacial water on gold electrodes studied by x-ray absorption spectroscopy *Science* **346** 831–4

[31] Arthur T S, Glans P A, Matsui M, Zhang R, Ma B and Guo J 2012 Mg deposition observed by *in situ* electrochemical Mg K-edge x-ray absorption spectroscopy *Electrochem. Commun.* **24** 43–46

[32] Scherzer M, Girgsdies F, Stotz E, Willinger M G, Frei E, Schlögl R, Pietsch U and Lunkenbein T 2019 Electrochemical surface oxidation of copper studied by *in situ* grazing incidence x-ray diffraction *J. Phys. Chem.* C **123** 13253–62

[33] Bak S M, Shadike Z, Lin R, Yu X and Yang X Q 2018 In situ/operando synchrotron-based x-ray techniques for lithium-ion battery research *NPG Asia Mater.* **10** 563–80

[34] Farmand M *et al* 2019 Electrochemical flow cell enabling: operando probing of electrocatalyst surfaces by x-ray spectroscopy and diffraction *Phys. Chem. Chem. Phys.* **21** 5402–8

[35] Bora D K, Glans P-A, Pepper J, Liu Y-S, Du C, Wang D and Guo J-H 2014 An ultra-high vacuum electrochemical flow cell for in situ/operando soft x-ray spectroscopy study *Rev. Sci. Instrum.* **85** 043106

[36] Kolmakov A, Dikin D A, Cote L J, Huang J, Abyaneh M K, Amati M, Gregoratti L, Günther S and Kiskinova M 2011 Graphene oxide windows for *in situ* environmental cell photoelectron spectroscopy *Nat. Nanotechnol.* **6** 651–7

[37] Weatherup R S 2018 2D material membranes for operando atmospheric pressure photoelectron spectroscopy *Top. Catal.* **61** 2085–102

[38] Velasco-velez J J *et al* 2016 Atmospheric pressure x-ray photoelectron spectroscopy apparatus : bridging the pressure gap *Rev. Sci. Instrum.* **87** 053121

[39] Xiang C, Papadantonakis K M and Lewis N S 2016 Principles and implementations of electrolysis systems for water splitting *Mater. Horiz.* **3** 169–73

[40] Paidar M, Fateev V and Bouzek K 2016 Membrane electrolysis—history, current status and perspective *Electrochim. Acta* **209** 737–56

[41] Wang Y, Ruiz D D F, Chen K S, Wang Z and Adroher X C 2020 Materials, technological status, and fundamentals of PEM fuel cells—a review *Mater. Today* **32** 178–203

[42] Favaro M, Abdi F, Crumlin E, Liu Z, van de Krol R and Starr D 2019 Interface science using ambient pressure hard x-ray photoelectron spectroscopy *Surfaces* **2** 78–99

J. Phys. D: Appl. Phys. **54** (2021) 124003

J-J Velasco-Vélez *et al*

[43] Weingarth D, Foelske-Schmitz A, Wokaun A and Kötz R 2011 *In situ* electrochemical XPS study of the Pt/[EMIM][BF4] system *Electrochem. Commun.* **13** 619–22

[44] Booth S G, Tripathi A M, Strashnov I, Dryfe R A W and Walton A S 2017 The offset droplet: a new methodology for studying the solid/water interface using x-ray photoelectron spectroscopy *J. Phys.: Condens. Matter* **29** 454001

[45] Starr D E, Favaro M, Abdi F F, Bluhm H, Crumlin E J and van de Krol R 2017 Combined soft and hard x-ray ambient pressure photoelectron spectroscopy studies of semiconductor/electrolyte interfaces *J. Electron Spectros. Relat. Phenom.* **221** 106–15

[46] Schulz K, Schmack R, Klemm H W, Kabelitz A, Schmidt T, Emmerling F and Kraehnert R 2017 Mechanism and kinetics of hematite crystallization in air: linking bulk and surface models via mesoporous films with defined nanostructure *Chem. Mater.* **29** 1724–34

[47] Arinchtein A, Schmack R, Kraffert K, Radnik J, Dietrich P, Sachse R and Kraehnert R 2020 Role of water in phase transformations and crystallization of ferrihydrite and hematite *ACS Appl. Mater. Interfaces* **12** 38714–22

[48] Bernsmeier D, Bernicke M, Schmack R, Sachse R, Paul B, Bergmann A, Strasser P, Ortel E and Kraehnert R 2018 Oxygen evolution catalysts based on Ir–Ti mixed oxides with templated mesopore structure: impact of Ir on activity and conductivity *Chem. Sus. Chem.* **11** 2367–74

[49] Bernicke M, Ortel E, Reier T, Bergmann A, Ferreira De Araujo J, Strasser P and Kraehnert R 2015 Iridium oxide coatings with templated porosity as highly active oxygen evolution catalysts: structure-activity relationships *Chem. Sus. Chem.* **8** 1908–15

[50] Ortel E, Reier T, Strasser P and Kraehnert R 2011 Mesoporous IrO$_2$ films templated by PEO-PB-PEO block-copolymers: self-assembly, crystallization behavior, and electrocatalytic performance *Chem. Mater.* **23** 3201–9

[51] Menzel N, Ortel E, Mette K, Kraehnert R and Strasser P 2013 Dimensionally stable Ru/Ir/TiO$_2$-anodes with tailored mesoporosity for efficient electrochemical chlorine evolution *ACS Catal.* **3** 1324–33

[52] Geiger S *et al* 2018 The stability number as a metric for electrocatalyst stability benchmarking *Nat. Catal.* **1** 508–15

[53] Velasco-Vélez J J *et al* 2018 The electro-deposition/dissolution of CuSO$_4$ aqueous electrolyte investigated by *in situ* soft x-ray absorption spectroscopy *J. Phys. Chem.* B **122** 780–7

[54] Boo H, Park S, Ku B, Kim Y, Park J H, Kim H C and Chung T D 2004 Ionic strength-controlled virtual area of mesoporous platinum electrode *J. Am. Chem. Soc.* **126** 4524–5

[55] Favaro M 2020 Stochastic analysis of electron transfer and mass transport in confined solid/liquid interfaces *Surfaces* **3** 392–407

[56] Stoerzinger K A, Favaro M, Ross P N, Hussain Z, Liu Z, Yano J and Crumlin E J 2018 Stabilizing the meniscus for operando characterization of platinum during the electrolyte-consuming alkaline oxygen evolution reaction *Top. Catal.* **61** 2152–60

[57] Novotny Z *et al* 2020 Probing the solid-liquid interface with tender x rays: a new ambient-pressure x-ray photoelectron spectroscopy endstation at the Swiss Light Source *Rev. Sci. Instrum.* **91** 023103

[58] Favaro M, Yang J, Nappini S, Magnano E, Toma F M, Crumlin E J, Yano J and Sharp I D 2017 Understanding the oxygen evolution reaction mechanism on CoO$_x$ using operando ambient-pressure x-ray photoelectron spectroscopy *J. Am. Chem. Soc.* **139** 8960–70

[59] Agrestini S *et al* 2017 Electronically highly cubic conditions for Ru in α-RuCl$_3$ *Phys. Rev.* B **96** 161107

[60] Kim D H *et al* 2015 Correlation between Mn and Ru valence states and magnetic phases in SrMn$_{1-x}$Ru$_x$ O$_3$ *Phys. Rev.* B **91** 075113

[61] Hu Z, von Lips H, Golden M, Fink J, Kaindl G, de Groot F M F, Ebbinghaus S and Reller A 2000 Multiplet effects in the Ru x-ray-absorption spectra of Ru(IV) and Ru(V) compounds *Phys. Rev.* B **61** 5262–6

[62] Frazer B H, Gilbert B, Sonderegger B R and De Stasio G 2003 The probing depth of total electron yield in the sub-keV range: TEY-XAS and X-PEEM *Surf. Sci.* **537** 161–7

[63] Shard A G 2012 A straightforward method for interpreting XPS data from core-shell nanoparticles *J. Phys. Chem.* C **116** 16806–13

[64] Shard A G, Wang J and Spencer S J 2009 XPS topofactors: determining overlayer thickness on particles and fibres *Surf. Interface Anal.* **41** 541–8

[65] Strocov V N 2013 Optimization of the X-ray incidence angle in photoelectron spectrometers *J. Synchrotron Radiat.* **20** 517–21

[66] Velasco-Vélez J J *et al* 2019 Electrochemically active Ir NPs on graphene for OER in acidic aqueous electrolyte investigated by *in situ* and ex situ spectroscopies *Surf. Sci.* **681** 1–8

[67] Trzhaskovskaya M B, Nefedov V I and Yarzhemsky V G 2002 Photoelectron angular distribution parameters for elements Z = 55 to Z = 100 in the photoelectron energy range 100–5000 eV *At. Data Nucl. Data Tables* **82** 257–311

[68] Trzhaskovskaya M B, Nefedov V I and Yarzhemsky V G 2001 Photoelectron angular distribution parameters for elements Z=1 to Z=54 in the photoelectron energy range 100–5000 eV *At. Data Nucl. Data Tables* **77** 97–159

[69] Schmickler W 2020 Double layer theory *J. Solid State Electrochem.* **24** 2175–6

[70] Jiang G, Cheng C, Li D and Liu J Z 2016 Molecular dynamics simulations of the electric double layer capacitance of graphene electrodes in mono-valent aqueous electrolytes *Nano Res.* **9** 174–86

[71] Wu C H, Pascal T A, Baskin A, Wang H, Fang H T, Liu Y S, Lu Y H, Guo J, Prendergast D and Salmeron M B 2018 Molecular-scale structure of electrode-electrolyte interfaces: the case of platinum in aqueous sulfuric acid *J. Am. Chem. Soc.* **140** 16237–44

[72] Weatherup R S, Eren B, Hao Y, Bluhm H and Salmeron M B 2016 Graphene membranes for atmospheric pressure photoelectron spectroscopy *J. Phys. Chem. Lett.* **7** 1622–7